Developing the Model Reduction Framework in High Frame Rate Visual Tracking Environment

Abdul Rozak Rivai Fassah, Abdul; Mkhoyan, T.; de Visser, C.C.; De Breuker, R.

DOI
10.2514/6.2021-0663

Publication date
2021

Document Version
Final published version

Published in
AIAA Scitech 2021 Forum

AIAA SciTech Forum
11–15 & 19–21 January 2021, VIRTUAL EVENT
AIAA Scitech 2021 Forum

10.2514/6.2021-0663

Developing the Model Reduction Framework in High Frame Rate Visual Tracking Environment

Abdul R.R. Fassah,*Tigran Mkhoyan,†Coen C. de Visser,‡Roeland de Breuker,§
Delft University of Technology, Delft, The Netherlands

The developments in the field of aerospace materials and structures allow the more light weight air vehicles. However, the aircraft body, particularly wing, can deform more appreciably due to the occurrence of flow separation and flutter. Therefore, active control is necessary in order to maintain structural integrity. One of the proposed control methods uses visual tracking for structural state estimation, which reduces complexity in terms of hardware and data processing requirements compared to the conventional method using inertial measurement units and gyroscopes. However, the wing displacement measurement involves a high number of states to estimate. An idea is to implement a model reduction method to be implemented as a mathematical model of the aeroelastic wing to quicken the state estimation process. The proposed method of model reduction by using Modified Frequency-Limited Model Reduction (MFLMR) method by Gugercin and Antoulas (2004) is then augmented with the application of singular perturbation step and validated with simulation in stochastic Gaussian gust regimes for two wing models. The effect of additional singular perturbation step is presented. The results show that the proposed MFLMR method with singular perturbation prevails to provide reliable representation of the true model in the simulated condition with different wing models in both time domain and frequency domain. Further analysis is recommended to be focused on the implementation of the proposed model reduction method to the state and parameter estimation in order to maintain the high sample rate that can be attained by using the controller scheme with visual tracking.

Nomenclature

M_α	= Pitching moment	Z	= Vertical force
I_α	= Wing moment of inertia	S_α	= Wing's static unbalance
M	= Mass	C_α, K_α	= Damping, stiffness (main wing)
$h, \dot{h}, \ddot{h}$	= Heaving attitude, rate, and acceleration	$\alpha, \dot{\alpha}, \ddot{\alpha}$	= Angle-of-attack attitude, rate, and acceleration
M_a	= Additional mass matrix due to aerodynamics	C_a	= Additional damping matrix due to aerodynamics
K_a	= Additional stiffness matrix due to aerodynamics	M_s	= Structural mass matrix
C_s	= Structural damping matrix	K_s	= Structural stiffness matrix
ws	= Subscript, wing section's structural parameters	$\vec{\mathbf{F}}_a$	= Aerodynamic forces and moments matrix
z_i	= Aerodynamic lag states	K_z	= Aerodynamic lag parameter matrix
b	= Half chord length	a	= Axis of rotation to wing's half-chord
V	= Airspeed	ρ	= Air density
θ	= Pitch angle	ζ	= Damping coefficient
$\phi, \ddot{\phi}$	= Roll angular attitude and rate	$\psi, \ddot{\psi}$	= Yaw angular attitude and rate

*M.Sc student, Faculty of Aerospace Engineering, Control and Operations Department, afassah@tudelft.nl, P.O. Box 5058, 2600GB Delft, The Netherlands.

†Ph.D. student, Faculty of Aerospace Engineering, Aerospace Structures and Materials Department, T.Mkhoyan@tudelft.nl, P.O. Box 5058, 2600GB Delft, The Netherlands.

‡Assistant Professor, Faculty of Aerospace Engineering, Control and Operations Department, C.C.deVisser@tudelft.nl, P.O. Box 5058, 2600GB Delft, The Netherlands

§Associate Professor, Faculty of Aerospace Engineering, Aerospace Structures and Materials Department, R.DeBreuker@tudelft.nl, P.O. Box 5058, 2600GB Delft, The Netherlands.

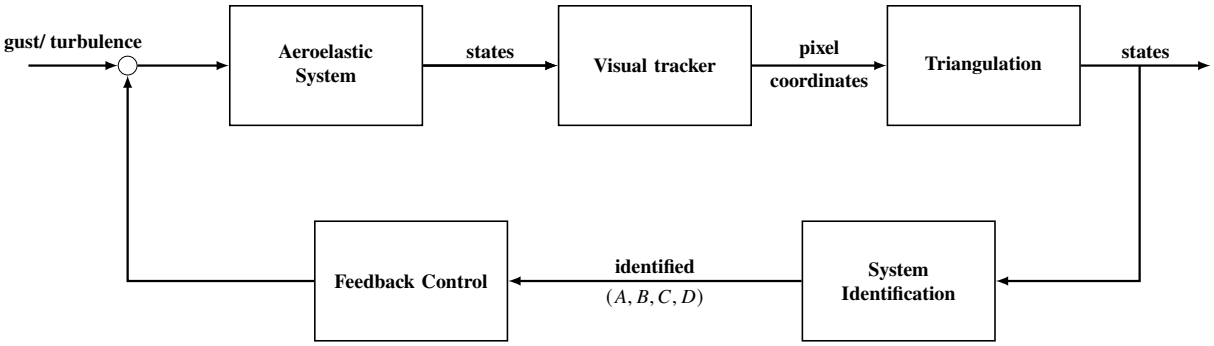

Figure 1 Controller scheme of an aeroelastic wing.

$x, \ddot{x}$	= Surge attitude and rate	$y, \ddot{y}$	= Sway attitude and rate
$\mathbf{A}_{red}$	= Balanced realization of $\boldsymbol{A}$ state-space matrix	$\mathbf{B}_{red}$	= Balanced realization of **B** state-space matrix
$\mathbf{C}_{red}$	= Balanced realization of **C** state-space matrix	$\mathbf{D}_{red}$	= Balanced realization of **D** state-space matrix
x_{true}	= True model states value	μ	= Mean
σ	= Standard deviation	red	= Subscript, of reduced model
$true$	= Subscript, true/ reference model	N	= Number of samples
$e(t)$	= Error of the sample	α_{95}	= 95% confidence interval

I. Introduction

In recent years, the development in the aerospace material and structural science has been bringing a breakthrough for the construction of air vehicles, which allows the expansion of aircraft size constraints. However, the aircraft body can deform more appreciably due to the occurrence of flow separation due to gust or turbulence, which can result in the degradation of the aircraft's handling qualities [1]. Fluttering and buffeting are two types of nonlinear input that may cause deformation due to energy loss to the aerodynamic flow. When the displacement does not converge, the structural disintegration can then occur ([2], [3]). In general, an aircraft component of a higher aspect ratio tends to deform more easily under such external force, namely wing. Therefore, a control scheme is developed to maintain structural integrity during the fluttering condition while the aircraft's handling qualities are satisfied. An aeroelastic estimation routine is needed to reconstruct the displacement states of the flexible aircraft structure such that a more accurate state observation can be used to identify the governing state-space of the aeroelastic model. The identified state-space can then become input for the controller's feedback, as mentioned earlier, dedicated to maintaining the flexible aircraft structure's integrity, namely wing. In order to monitor and control the displacement, one of the proposed methods is by a combination of the visual tracking method. This method reduces the complexity of hardware and data processing compared to the conventional method of planting inertial measurement units and gyroscopes in wing sections. The scheme of the controller for the aeroelastic structure is depicted in Figure 1.

The proposed novel method to replace conventional inertial measuring units across the wing is by exploiting the advancement of computer vision science. That is by using a camera measurement. In such a configuration, the camera measures each wing section's angular and translation position by tracking the position of a target object or a marker attached to the wing section. Visual tracking has been used in various studies and has been successfully implemented on wind tunnel models in early studies [4]. It also has seen wide application in robot manipulation [5]. In recent years, however, embedded hardware capabilities have significantly advanced, and demanding computer vision algorithms can run onboard and on-line in a compact hardware configuration ([6],[7]). Visual tracking can also greatly increase the robustness by coupling it with a state estimation routine. This coupling allows the tracker to handle occlusions due to the camera's low resolution or estimate the tracker's motion trajectory under marker loss. Hence, it is required for the system to reconstruct the motion trajectory and apply the Kalman filtering. Trajectory reconstruction and visual tracking have been successfully demonstrated in previous studies by Mkhoyan et al. ([8, 9]).

For identification and control purposes, however, it is relevant to reconstruct the displacements of a flexible structure and identify the underlying state-space of the system. When this can be done on-line, the identified state-space model can be used to deploy an adaptive control strategy of the aeroelastic wing structure (e.g., control surface such as flaps, to

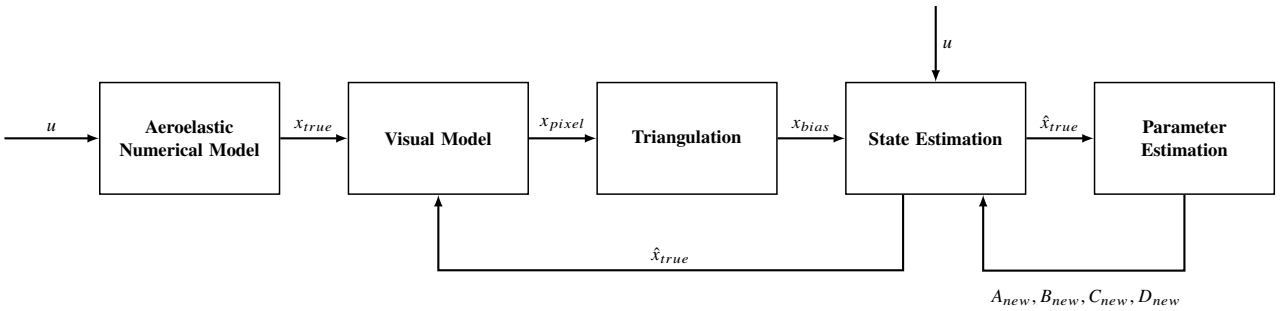

Figure 2 Open-loop process of the controller scheme.

stabilize the aeroelastic wing from the structural failure due to the excessive deformation).

However, due to the nature of an aeroelastic structure's displacement modes, the measurement will have to be conducted at numerous wing sections simultaneously. The increase in the number of analyzed wing sections and its degrees of freedom will also increase the number of states. Moreover, the deformation modes of an aeroelastic wing will require the measurement to be computed at a high sampling rate. Hence, the increase in the number of states to estimate will increase the computational burden, which hinders the utilization of a high sampling rate system. The realization of the state-space for an aeroelastic structure should be then reduced with smaller representation; hence the computational cost for the controller will be cheaper, thence faster. In this paper, the reduction methods of the state-space will be explored to allow the use of the controller with a high frame-rate visual tracker to implement a fast control feedback loop.

A. Paper structure

The focus of this paper is to analyze and develop possible common model reduction methods to enable the quick state estimation coupled with a high frame rate visual tracker. Therefore, in the end, the proposed model reduction will be implemented to reduce the state-space size of the state estimator as part of an aeroelastic wing controller scheme with visual tracking. For the paper's focus, the visual model, which represents the physical representation of the wing and the embedded fast visual tracking routine, will be put aside. Hence, the triangulation will be put aside. The following Section II presents the introduction to the whole tracking framework (Figure 1) in more detail and is followed by the derivation of the equation of motion of the aeroelastic model with its contributing states as the basics to construct the full realization of aeroelastic wing system state-space. Section III discusses the common methods of model reduction in aeroelastic structure numerical experiments with the experimental concern of the camera tracking system's limitations, such as the sampling rate. The suitable model reduction method will be chosen and developed to accommodate a quicker state estimation with a reduced state-space for a high rate controller scheme with a visual tracking environment from which the derived equation of motion can then be reduced. Therefore, to support the full numerical simulation scheme's application as in Figure 1, the paper will investigate the aeroelastic mathematical modeling reduction part. The performance and the development of the proposed model reduction method will be compared with the founding method. The experiment setup will be yielded, and the results of the comparison study will be presented and discussed in Section IV. In the end, the paper concludes in Section V.

II. Framework and Basic Equation of Motion

A. Full Controller Scheme

A closer look at the open-loop control scheme can be seen in Figure 2. The bracket is the tool used in order to create the full numerical simulation of the scheme.

1. Visual Tracking

The first building block of the planned control system is the high frame rate, visual tracker. The reason for using a high frame rate visual tracker is because of the nature of the deformation modes of the structure, which occurs at high frequency. The visual tracker is used to identify the flexible wing structure's deformation caused by the dynamics excited by the aerodynamic gust or turbulence.

With the advancement of computer vision technology, the tracker's high frame rate can accommodate the observation of the first modes of deformation; those are at a lower frequency. In general, a fast-tracking system uses the identification of features like edges, corners, or blobs (a feature that has an area) on the image as the basis for the tracking. This feature-based tracking has been developed.

The first developed routine called fragment tracking was developed by Lucas and Kanade [10], and Shi [11]. However, the tracking is constrained by the transformation of the feature perspective of the image. The object displacement causes this change that, in turn, changes the shape of the features attached. Hence, this will cause drift of the tracker. Color-based tracking [12] was meant to mitigate the object transformation problem. Here, the color histogram becomes the object of the minimization problem to determine the exact object position. In this problem, the distance of the referred color histogram should be minimal compared to the candidate tracker position in the proceeding frames. Despite the advancements, however, the constraint remains as the color distribution is the tracker's determining variable. Since the object is "blurred" with the color kernel, it is harder for the tracker to detect the abrupt moves and the object's features. More recently, the correlation-filter (CF) based tracker is developed for the feature tracking routine. In general, the CF routine divides the training image into subwindows with a predetermined target or object of interest. These subwindows can then be labeled or weighted such that the target position can then be acquired. The weight or the subwindow's classifier will be positive if the subwindow has a high overlap with the ground truth, while the contrary will be given for subwindow far or lowly correlate with the ground truth or target. The following figure depicts the cross-correlation process in the tracker routine.

A more recent algorithm developed is Kernelized Correlation Filter [13], which tracks based on the histogram of oriented gradients (HOG) of the object of interest; this allows the routine to run at approximately 130-150 Hz with an accuracy of more than 90 percent [14]. However, the routine's accuracy is still hampered by the occlusion problem. This problem can be mitigated with the combination of a visual tracker routine with state estimation. It is exemplified by combination of visual tracker with Kalman Filter routine in pixel reference frame as in [15],[16], and [17].

However, since the pixel unit by itself is an area, the extracted position in the world reference frame will also have uncertainties in terms of the object's exact position. Therefore, the proposed approach is tailored to increase the accuracy of the closed-loop controller scheme of the aeroelastic wing where the movement of displacement is calculated based on real-time state and parameter estimation by using the aeroelastic mathematical model instead of using the raw pixel reference frame position in order to determine the displacement of the wing sections.

2. State and Parameter Identification

As previously established in the introduction, the wing can deform due to turbulence. It could also happen that the structure may suffer such deformation from fatigue due to continuous long exposure to the aerodynamic forces and moments. Fluttering, in a mathematical sense, happens due to the loss in terms of damping. Therefore, it is necessary to know the change while the aircraft is under such forces. The system identification process of a system serves as the channel to determine the structure of the numerical state-space system, e.g., the aeroelastic structure system, which can then be used to determine the feedback to control the deformation of the structure with the control surface. The process itself is divided into two main parts, state estimation and parameter estimation. In this framework, the state estimation serves two critical functions. First, it enhances the tracking's quality by correcting the true position of the tracker, and secondly, to provide the basics to calculate the unknown parameters needed to reconstruct the state-space of the aeroelastic wing.

While the choice for state estimation is many, the Kalman Filter routine is more favorable to be coupled with the computing visual tracking routine, in this case, KCF. Ghanem and Shinozuka (1994) ([18],[19]) propose and analyze three possible methods that enable the parameter estimation in real-time: Extended Kalman Filter (EKF) approach, Recursive Least-Square (RLS) approach, and Maximum Likelihood Estimation (MLE) approach.

From the reported results, it can be seen that both the MLE and EKF approach provides better reliability in the calculation. However, augmenting the Kalman Filter to include the parameter estimation cause the coupling of the parameters and the states, which can slow the process. The MLE routine is then simplified using three approaches, namely Filter Error, Output Error, and Equation Error [20]. In Equation Error and Output Error, the methods respectively dismiss measurement errors and process noise. The Filter Error approach of MLE considers both the process noise and measurement noise, hence requiring no further modification to obtain unbiased estimation. The Filter Error approach method can be simplified in the Two-Step Method [21]. In this method, the MLE criteria can be achieved by dividing it into two parts. First, the object's dynamics need to be reconstructed and cleared up from the process and measurement noise by the implementation of the Kalman Filter. Next, the Recursive Least Square routine can then be coupled to

obtain the actual parameters as the wing structure condition or state-space update in numerical terms. This approach is used to avoid the use of augmenting the Kalman Filter state space that burdens the computational cost for estimating parameters.

B. Aeroelastic Wing Dynamics

1. Typical Section Structural Dynamics

In order to construct the full state-space of the aeroelastic wing, the basics of the aeroelastic wing's equation of motion will be derived. The full equations of motion will become the basis for the initial model to be reduced in the simulation. The equations of motion of typical wing section have been formulated by Theodorsen in the form of a spring-mass harmonic behavior equation [22]. The equation is then improved to represent the damped behavior of a wing in reality as observed by papers such as [23],[2], and [24]. Hence, Theodorsen's equation of motion for the clean wing as

$$\begin{aligned} M_\alpha &= I_\alpha \ddot{\alpha} + S_\alpha \ddot{h} + C_\alpha \dot{\alpha} + K_\alpha \alpha \\ Z &= S_\alpha \ddot{\alpha} + M\ddot{h} + C_h \dot{h} + K_h h \end{aligned} \tag{1}$$

However, it can be seen from the equation above that the aerodynamic influence is not clearly stated through the representation in the time domain. The aerodynamic property through which the aircraft structure is excited also influences the behavior of the structure. Leishman and Nguyen [25] then introduce the two-dimensional wing dynamics model in the time domain by taking into account the aerodynamic effect on the structure obtained from the identification of Wagner's indicial response function. Hence the state-space of an aeroelastic wing dynamics can be represented in a state-space form in the integration of structural and aerodynamic influence [26] which is rewritten here as

$$\mathbf{F}_a = (M_a + M_s)\ddot{x}_s + (C_a + C_s)\dot{x}_s + (K_a + K_s)x_s + K_z z_i \tag{2}$$

Where $\mathbf{F}_a$ represents the external force and moment inputs, and the states are x_s, whereas z_i represents the aerodynamic "stiffness" lag states due to trailing circulatory lift and the K_z represents the aerodynamic lag matrix. The M_s, C_s, K_s represent the structure influence matrix as derived in the previous subsection. M_a, C_a, K_a represent the aerodynamic influence to the total "mass," damping, and stiffness, respectively. The occurrence of the three latter matrices is due to the circulatory influence on the angular attitude of the wing. De Breuker et al. point out the influence of the circulatory lift to the produced lift coefficient and therefore the moment also resulted as the production of the additional lift. The details can be referred back in their paper [26].

2. Aeroelastic Clamped Wing Dynamics

With the full identification of structural and aerodynamic influence to the wing displacement, the full mathematical model of two-dimensional wing structure motion can then be fully formulated to become

$$\begin{aligned} &(M_a + M_s)\ddot{x}_s + (C_a + C_s)\dot{x}_s + (K_a + K_s)x_s + K_z z_i = \mathbf{F}_a \\ &\begin{bmatrix} I_\alpha & S_\alpha \\ S_\alpha & M \end{bmatrix} \begin{bmatrix} \ddot{\alpha} \\ \ddot{h} \end{bmatrix} + \begin{bmatrix} C_\alpha + (\frac{1}{2}\rho V S(b(\frac{1}{2}+a))^2\pi) & 0 \\ (\frac{1}{2}\rho V S(b(\frac{1}{2}+a))\pi) & C_h \end{bmatrix} \begin{bmatrix} \dot{\alpha} \\ \dot{h} \end{bmatrix} + \begin{bmatrix} K_\alpha + (\frac{1}{2}\rho V^2 S(b(\frac{1}{2}+a))\pi) & 0 \\ (\frac{1}{2}\rho V^2 S\pi) & K_h \end{bmatrix} \begin{bmatrix} \alpha \\ h \end{bmatrix} \\ &+ \begin{bmatrix} \frac{1}{2}\rho V^2 S(b(\frac{1}{2}+a))(4\pi\frac{b_1 b_2}{2}(\frac{V}{b})^2) & \frac{1}{2}\rho V^2 S(b(\frac{1}{2}+a))(A_1 b_1 + A_2 b_2)(\frac{V}{b}) \\ \frac{1}{2}\rho V^2 S(4\pi\frac{b_1 b_2}{2}(\frac{V}{b})^2) & \frac{1}{2}\rho V^2 S(A_1 b_1 + A_2 b_2)(\frac{V}{b}) \end{bmatrix} \begin{bmatrix} z_1 \\ z_2 \end{bmatrix} = \begin{bmatrix} M_\alpha \\ Z \end{bmatrix} \end{aligned} \tag{3}$$

The solution can then be expanded into a three-dimensional wing solution by dividing the wing-body into several wing sections connected through the spring and dampers [27]. In a three-dimensional wing model, there are six degrees of freedom consisting of three angular (ϕ, α, ψ) and three translation (x, y, h) degrees of freedom for each wing sections.

Thence, for each wing section, the full mathematical model becomes

$$\begin{bmatrix} M_\phi \\ M_\alpha \\ M_\psi \\ F_x \\ F_y \\ F_z \end{bmatrix}_i = M_{ws}\ddot{x}_s + C_{ws}\dot{x}_s + K_{ws}x_s + \begin{bmatrix} 0 & 0 \\ \frac{1}{2}\rho V^2 S(b(\frac{1}{2}+a))(4\pi\frac{b_1 b_2}{2}(\frac{V}{b})^2) & \frac{1}{2}\rho V^2 S(b(\frac{1}{2}+a))(A_1 b_1 + A_2 b_2)(\frac{V}{b}) \\ 0 & 0 \\ 0 & 0 \\ 0 & 0 \\ \frac{1}{2}\rho V^2 S(4\pi\frac{b_1 b_2}{2}(\frac{V}{b})^2) & \frac{1}{2}\rho V^2 S(A_1 b_1 + A_2 b_2)(\frac{V}{b}) \end{bmatrix} \begin{bmatrix} z_{1,i} \\ z_{2,i} \end{bmatrix}$$
$$+ \begin{bmatrix} 0 & 0 \\ \frac{1}{2}\rho V^2 S(b(\frac{1}{2}+a))\pi & \frac{1}{2}\rho V S(b(\frac{1}{2}+a))^2\pi \\ 0 & 0 \\ 0 & 0 \\ 0 & 0 \\ \frac{1}{2}\rho V^2 S\pi & \frac{1}{2}\rho V S(b(\frac{1}{2}+a))\pi \end{bmatrix} \begin{bmatrix} \alpha_i \\ \dot{\alpha}_i \end{bmatrix} \tag{4}$$

where $z_{1,i}$ and $z_{2,i}$ represents the aerodynamic lag states belonging solely to the corresponding wing section and $\dot{\alpha}_i$ and α_i are displacement attitude and rates are belonging solely to the corresponding i^{th}-wing section. These aerodynamic states are also not constant as their parameters' values change with the change of the aerodynamic profile and the quasi-steady angular attitude of each wing section. The formulation of the aerodynamic lag derivatives can be further consulted in the paper by De Breuker et al. [26]. Notice that the angle of attack term is used instead of pitch angular attitude. The pitch angle of wing section can be obtained by the formula of [27]

$$\theta = \alpha - \frac{\dot{h}}{V} \tag{5}$$

III. Aeroelastic Wing Model Reduction for Limited Frequency Band

A model reduction is paramount to keep the sampling rate high by cutting the computational cost by reducing the number of states to calculate for each iteration for a large state-space due to numerous sampling points across the wingspan. However, it is also desirable that the reduced model provides reliable measurement compared to the wing's actual response.

Gillebaart and de Breuker [28] has tabulated and reviewed the four most popular model order reduction to solve unsteady aerodynamics state-space. In another paper by Besselink et al. [29], few other methods are presented and reviewed for its application in structural dynamics, numerical computation, and in control. The two papers provide the methods of model order reduction, these are:

1. Modal truncation (MT) ([30],[31]),
2. Balanced truncation (BT) [32],
3. Proper Orthogonal Decomposition (POD) [33],
4. Balanced Proper Orthogonal Decomposition (BPOD) ([34],[35]), and
5. Krylov subspace model order reduction (KMOR) ([36],[37]).

Based on the two papers' results and conclusion, the MT and KMOR method (named otherwise as moment matching method) is computationally cheaper compared to the BT method. Gillebaart and de Breuker further approve that BT is computationally the costliest among the presented methods, despite it being limited to use BT for a moderate-sized problem. However, BT and MT are more reliable since it guarantees the preservation of the stability of the true model in the reduced state-space realizations. Furthermore, the BT method is also bounded by apriori error criteria. These characteristics are not possessed by other methods that their results' accuracy needs to be investigated further [29]. The remaining POD and BPOD model reduction methods also yield accurate results. However, the error margin, which

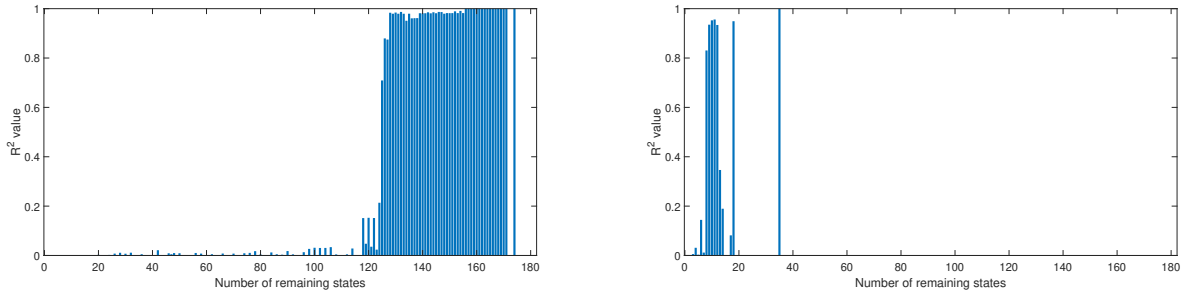

(a) Moore's balanced truncation method. **(b) Frequency-limited Gawronski-Juang balanced truncation method.**

Figure 3 R-squared value of model reduction iteration with respective Moore and Gawronski-Juang's methods.

bounds the balanced realization error of BPOD, needs to be fine-tuned. The error margin tuning makes the method less robust, while POD does not guarantee the stability of its true state-space [28]. The BT method is very robust in characteristics as the method requires no input other than the required order of the ROM; this makes the method one of the most widely used model reduction methods. Although computationally costlier at $O(n^3)$, since the number of the states introduced in this report is in order of 10^2 and computed before the implementation of the Two-Step Method, the BT computational cost is acceptable [38]. Furthermore, it is found that the balanced truncation method is the most popular model reduction method. The method preserves the full high-order model's stability and maintains the reduced model within a priori error bound. The successfully reduced realization of the true identified aeroelastic wing state-space model will be then used as the observation model for the state estimation routine.

Moore [32] delivers the first balanced truncation algorithm. In short, balanced truncation is a technique that reduces the order of the model based on the energy or Hankel singular values of the system's controllability and observability Gramian values [39]. Hankel Singular Values or HSV is essentially the diagonal part of the singular matrix obtained from the singular value decomposition that will later be described in this section. The HSV shows the contribution of one state from the lowest to the largest, as shown in the graph. The idea is to discard the states with the lowest energy such that the actual model can then be represented with fewer states but still represent the true behavior.

Nevertheless, the realization applies to an infinite range of frequency and infinite time-domain data, which is impractical. In many cases, some measurement tools can only work at a certain range of frequencies. The model reduction algorithm success can be summarized by looking at the R^2 value of reduction realization iteration for Asjes wing model [27] with 182 states. The R-squared value measures how the true model can be well observed by the reduced model, with 1 signifies the full correlation or perfect observation of the true model, and 0 signifies that the reduced model cannot represent the true response. The calculation of R-squared value is equal to the squared Pearson correlation coefficient (ρ_P) of the true system and the reduced system, which is formulated as

$$\rho_P = \frac{1}{N-1}\sum_{i=1}^{N}\left(\frac{x_{i,true}-\mu_{true}}{\sigma_{true}}\right)\left(\frac{x_{i,red}-\mu_{red}}{\sigma_{red}}\right) \tag{6}$$

In this case, the heave state of the tip wing section will be presented. The following figures show the reduced model's accuracy with different state realization numbers ranging from the full realization of the true model to the realization with only one state remaining. It can be seen that Moore's balanced truncation method fails to produce a reliable (R^2 value near 1) reduced realization with less than 157 states. In other words, the reduced model representation only best approximates the true model response with several states close to the full number of states. Therefore, this signifies that the balanced truncation results in insignificant reduction because of the effort to equate the system's response at all frequencies and the presence of very fast deformation modes in it. Therefore, it degrades the quality of reduced model observation in the visual tracker operating frequency band. The graph of the R^2 value can be seen as in Figure 3a.

The first attempt to limit the effect of very fast-displacement modes has been taken by weighting the frequency range in the balanced truncation method by Enns [40]. The method is then further simplified by Gawronski and Juang, which removes the necessity of manually weighing the frequency range using frequency-domain Gramian representation [41].

However, since the frequency-limited controllability and observability Gramian matrices of Gawronski et al.'s are not guaranteed to be positive definite, this disables the routine to perform the Gramian decomposition. As consequence, the stability of the reduced model cannot be guaranteed ([42],[43]). Furthermore, Gawronski and Juang also do not

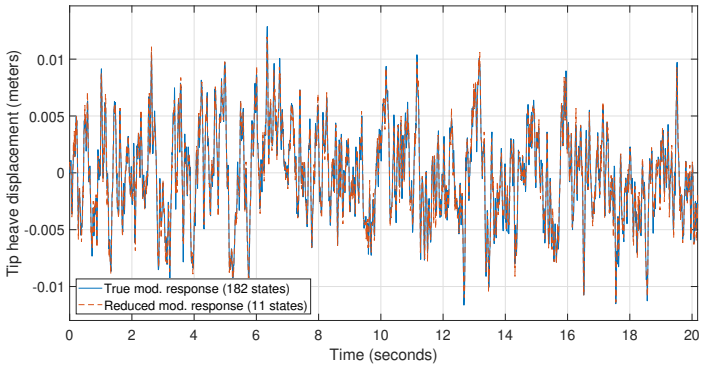

(a) Wingtip heave time response.

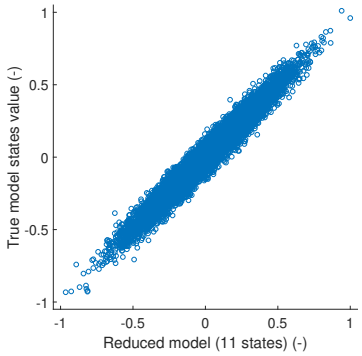

(b) Scatter plot of the heave position simulated by true model against the reduced model.

Figure 4 Time response and scatter plot from Gawronski-Juang's frequency-limited model reduction with 11 states.

guarantee the error bound of the reduced model. This is shown in the following Figure 3b. It can be seen that although Gawronski-Juang's routine is able to produce a reduced realization with a smaller number of remaining states, the success of the reduction cannot be guaranteed at all reduced realizations. This is shown on the graph with a blank bar at most of the realization of remaining states, with occasional reduction success at reduced realization less than 40 states, while the frequency-limited balanced truncation method fails to produce all reduced realization of a true model with more than 40 states. In this case, only the reduced realization with the order of 35 states attains R-squared value, while the second-best reduced realization is obtained with the realization of 11 states with the R-squared of 0.965. To further support the finding, an example of a time response of the wingtip section's heave state is presented in Figure 4. It can be seen that the heaving position simulated by the reduced model deviates from the true position, shown by some offsets in the graph.

A. Modified Frequency-Limited Model Reduction (MFLMR) Routine

The problem of the balanced realization in a limited frequency range then becomes the basis for Gugercin and Antoulas [42]. It is proposed that the solution to the non-positive definite controllability Gramians (W_c) and observability Gramians (W_o) matrices can be solved by performing the eigenvalue decomposition and solving the factorization through the Lyapunov-Cholesky routine (MATLAB command: "*lyapchol*"). The modified Gawronski-Juang's frequency-limited balanced truncation method can be formulated as follows:

1. Establish the lower and upper bound of frequency limit $[\omega_1, \omega_2]$,
2. Obtain controlability and observability Gramian matrix for all frequency by solving the Lyapunov equation [32],
3. Calculate the $S(\omega)$ term for lower and upper bound of frequency limit [41], formulated as

$$S(\omega) = \int_{-\omega}^{\omega} H(v)\frac{dv}{2\pi} = \frac{j}{2\pi} ln((j\omega I + \mathbf{A})(-j\omega I + \mathbf{A})^{-1} \tag{7}$$

4. Determine controlability and observability Gramian at lower and upper bound frequency $(W_c(\omega_1), W_c(\omega_2), W_o(\omega_1), W_o(\omega_2))$ where

$$\begin{aligned} W_c(\omega) &= W_c S^*(\omega) + S(\omega) W_c \\ W_o(\omega) &= S^*(\omega) W_o + W_o S \end{aligned} \tag{8}$$

5. Calculate the frequency-limited Gramian matrices, formulated as

$$\begin{aligned} W_c(\Omega) &= W_c(\omega_2) - W_c(\omega_1) \\ W_o(\Omega) &= W_o(\omega_2) - W_o(\omega_1) \end{aligned} \tag{9}$$

6. Identify the rank of $W_c(\Omega)$ as ρ_{W_c} and the rank of $W_o(\Omega)$ as ϱ_{W_o} Perform eigenvalue decomposition of frequency limited Gramian matrices [42] such that

$$\begin{aligned} W_c(\Omega) &= \mathbf{M}\Lambda\mathbf{M}^T \ , \ \Lambda = diag(\sigma_{c_1}, \cdots, \sigma_{c_N}) \\ W_o(\Omega) &= \mathbf{N}\Delta\mathbf{N}^T \ , \ \Delta = diag(\sigma_{o_1}, \cdots, \sigma_{o_N}) \end{aligned} \tag{10}$$

7. Calculate new $\hat{\mathbf{B}}$ and $\hat{\mathbf{C}}$ such that

$$\begin{aligned} \hat{\mathbf{B}} &= \mathbf{M}diag(|\sigma_{c_1}|^{1/2}, \cdots, |\sigma_{c_{\rho_{W_c}}}|^{1/2}, 0, \cdots, 0) \\ \hat{\mathbf{C}} &= \mathbf{N}diag(|\sigma_{o_1}|^{1/2}, \cdots, |\sigma_{o_{\varrho_{W_o}}}|^{1/2}, 0, \cdots, 0) \end{aligned} \tag{11}$$

8. Solve the factorization of modified frequency-limited controlability ($\bar{P}_\Omega$) and observability ($\bar{Q}_\Omega$) Gramian matrices through the solution of the equation

$$\begin{aligned} \mathbf{A}\bar{P}_\Omega + \bar{P}_\Omega\mathbf{A}^* + \hat{\mathbf{B}}\hat{\mathbf{B}}^* &= 0 \\ \mathbf{A}^*\bar{Q}_\Omega + \bar{Q}_\Omega\mathbf{A} + \hat{\mathbf{C}}^*\hat{\mathbf{B}} &= 0 \end{aligned} \tag{12}$$

whose Cholesky factorization are determined as

$$\begin{aligned} (\bar{P}_\Omega) &= \mathbf{P}\mathbf{P}^T \\ (\bar{Q}_\Omega) &= \mathbf{Q}^T\mathbf{Q} \end{aligned} \tag{13}$$

9. Given the matrix $\mathbf{H} = \mathbf{Q}\mathbf{P}$, perform the singular value decomposition of the matrix such that

$$\mathbf{H} = \mathbf{V}\mathbf{S}^2\mathbf{U}^T \tag{14}$$

where $\mathbf{V}^T\mathbf{V} = I$ and $\mathbf{U}^T\mathbf{U} = I$ and $\mathbf{S}$ is Gramian positive semi-definite diagonal matrix.

10. Calculate the transformation matrix and its inverse, where

$$\begin{aligned} \mathbf{T} &= \mathbf{P}\mathbf{U}\mathbf{S}^{-1} = \mathbf{Q}^{-1}\mathbf{V}\mathbf{S} \\ \mathbf{T}^{-1} &= \mathbf{S}\mathbf{U}^T\mathbf{P}^{-1} = \mathbf{S}^{-1}\mathbf{V}^T\mathbf{Q} \end{aligned} \tag{15}$$

and obtain the realization of the balanced realization of the model where

$$\begin{aligned} \bar{\mathbf{A}} &= \mathbf{T}^{-1}\mathbf{A}\mathbf{T} \\ \bar{\mathbf{B}} &= \mathbf{T}^{-1}\mathbf{B} \\ \bar{\mathbf{C}} &= \mathbf{C}\mathbf{T} \\ \bar{\mathbf{D}} &= \mathbf{D} \end{aligned} \tag{16}$$

11. Consider the model reduction to be conducted for the balanced state space (Step 6). Separate the state matrix into

$$x_b = \begin{bmatrix} x_{b1} & x_{b2} \end{bmatrix} \tag{17}$$

where x_{b_1} represents the states to be kept in the reduced model. Then the state space matrices are partitioned accordingly as

$$\begin{aligned} \bar{\mathbf{A}} &= \begin{bmatrix} \bar{\mathbf{A}}_{11} & \bar{\mathbf{A}}_{12} \\ \bar{\mathbf{A}}_{21} & \bar{\mathbf{A}}_{22} \end{bmatrix} \\ \bar{\mathbf{B}} &= \begin{bmatrix} \bar{\mathbf{B}}_1 \\ \bar{\mathbf{B}}_2 \end{bmatrix} \\ \bar{\mathbf{C}} &= \begin{bmatrix} \bar{\mathbf{C}}_1 & \bar{\mathbf{C}}_2 \end{bmatrix} \\ \bar{\mathbf{D}} &= \bar{\mathbf{D}} \end{aligned} \tag{18}$$

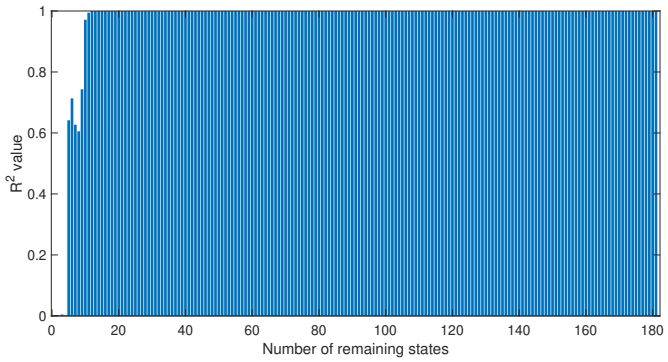

(a) R-squared value.

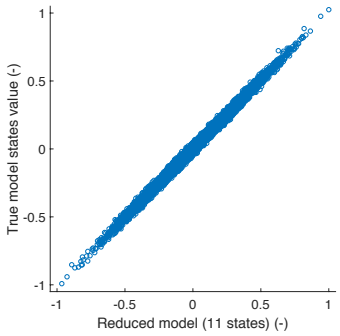

(b) Scatter plot with reduced model order of 11 states.

Figure 5 The R-squared of model reduction iteration and the scatter plot of reduced model of 11 states with MFLMR methods.

Hence the balanced truncated model (reduced state space model) becomes

$$\begin{aligned} \mathbf{A}_{red} &= \bar{\mathbf{A}}_{11} \\ \mathbf{B}_{red} &= \bar{\mathbf{B}}_{1} \\ \mathbf{C}_{red} &= \bar{\mathbf{C}}_{1} \\ \mathbf{D}_{red} &= \bar{\mathbf{D}} \end{aligned} \tag{19}$$

1. Preliminary Analysis

Using the same method, as shown in Figure 3, the reduced realization using the MFLMR method. The results in Figure 5a show that the reduced model iteration is much more successful compared to the two preceding methods. This result corresponds to the energy of the states in the system. As seen in Figure 6, the last ten states have significantly more energy compared to the other remaining states. Therefore, reducing the system realization order to less than ten will cause degradation in the reduced model's accuracy compared to the true model. In addition to that, a comparison can be derived from the Figure 4b and 5b. The comparison shows that the MFLMR performs more accurately than Gawronski-Juang's method.

Given the results of the singular value decomposition of the MFLMR method, it can be seen that the Hankel singular value of the modified balanced realization is closer to zero, as exemplified in Figure 6. It is also possible to use a singular perturbation method in order to obtain the realization of model reduction instead of direct partitioning of state-space matrices as presented through balanced truncation ([38],[44]). The difference is in the goal where the singular perturbation tries to achieve the equalization of steady-state gain of both the full model and the reduced model instead of equalizing the norm at infinite frequency. In other words, the goal of the singular perturbation method is to yield the best approximate of the true model at the lower frequency, in the opposite of that of the balanced truncation where it bounds the error at the infinite frequency.

In order to achieve this, the truncated state-space matrices are perturbed by the remaining matrix-part related to the rejected states ($\bar{x}_2$). Assuming the rejected states converges to a steady-state much faster than the remaining states $\bar{x}_1$. The derivative of the rejected states is set to zero [38]. This can be seen as the extension to the algorithm of the MFLMR. Given the partitioned matrix structure, the model reduction matrices resulted from singular perturbation method can be formulated as

$$\begin{aligned} \mathbf{A}_{red} &= \bar{\mathbf{A}}_{11} - (\bar{\mathbf{A}}_{12}\bar{\mathbf{A}}_{22}^{-1}\bar{\mathbf{A}}_{21}) \\ \mathbf{B}_{red} &= \bar{\mathbf{B}}_{1} - (\bar{\mathbf{A}}_{12}\bar{\mathbf{A}}_{22}^{-1}\bar{\mathbf{B}}_{2}) \\ \mathbf{C}_{red} &= \bar{\mathbf{C}}_{1} - (\bar{\mathbf{C}}_{2}\bar{\mathbf{A}}_{22}^{-1}\bar{\mathbf{A}}_{21}) \\ \mathbf{D}_{red} &= \bar{\mathbf{D}} - (\bar{\mathbf{C}}_{2}\bar{\mathbf{A}}_{22}^{-1}\bar{\mathbf{B}}_{2}) \end{aligned} \tag{20}$$

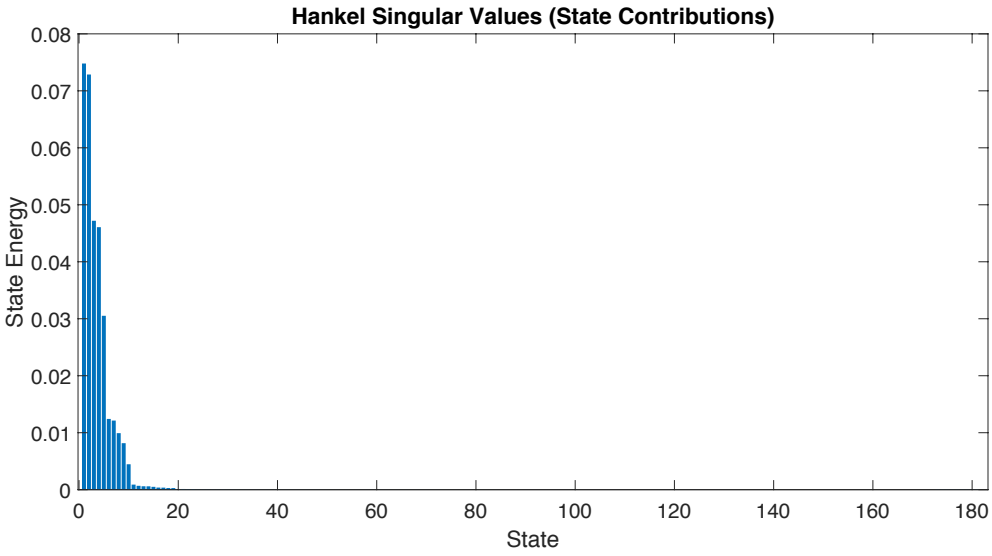

Figure 6 Hankel Singular Values of the MFLMR's balanced realization.

Table 1 Frequency Range of Visual Tracking System Case

Parameters	Value
Lower limit (ω_1)	0 Hz
Upper limit (ω_2)	150 Hz

IV. Results and Discussion

A. Experiment Setup

For the experiment scenario, the structure as modeled in Section III is perturbed with a discrete gust signal in the form of stochastic Gaussian forces and moments. The simple rectangular wing is the object with a symmetric airfoil type of NACA-0010. The matrix of structural wing's stiffness and mass matrices are derived from the modeling *Proteus* software, which has been developed by the Department Aerospace Structures and Materials, Delft University of Technology. The routine of software can be read further in the Ph.D. thesis of Werter [45]. In addition to that, the wing has geometric parameters of semi-span of 1.75 meters, length of chord 0.25 m, and shear center location of 0 meters from the aerodynamic center. The PROTEUS discretization program results in the division of the wing into 13 wing sections with 6 degrees of freedom. To solve the wing dynamics, a state-space of 182 by 182 states is then formed, including 156 structural states and derivatives and 26 aerodynamic lag states. The system matrix ("A" matrix) of the state-space has the form as shown in the following Figure 7. Each of the blue dots represents the non-zero parameters..

Two models of the structural model will be investigated, namely Model 1 and Model 2. The mathematical model of both models has a different representation of eigenvalues as shown in Figure 8. The difference lies in the realization of the damping system. The first system is by multiplying the double value of the damping coefficient (2ζ) times the natural frequency, and the second model is approached by Asjes' damping model formulated as

$$\omega_{n_{[27]}} = 2\zeta\sqrt{diag(K_s) \oslash diag(M_s)} \tag{21}$$

where the $\oslash$ represents the element-wise division operation, and the frequency upper and lower limit for the frequency-limited model reduction is chosen as of the Table 1. The time interval between each sampling is simulated at a frequency of 100 Hz.

A comparison study between the MFLMR's limited frequency balanced truncation with and without singular perturbation for the stochastic Gaussian gust condition of both Model 1 and 2 will be conducted to identify the advantage

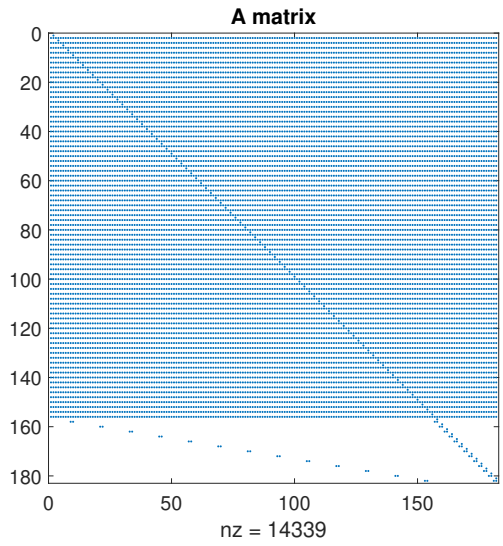

Figure 7 The state space's system matrix ("A" matrix).

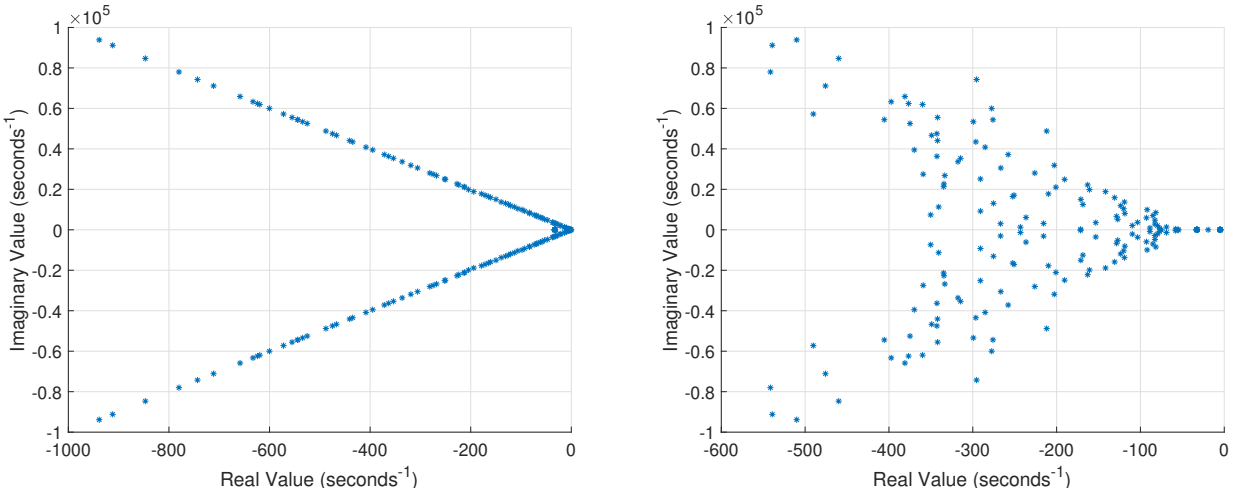

(a) Model 1. **(b) Model 2.**

Figure 8 Pole maps of Wing Model 1 and Wing Model 2.

of the implementation of singular perturbation step towards the model reduction results. For the sake of brevity, the following results will be focused on the behavior of the wingtip section's heave as the section is the farthest from the clamp, hence the most prone to structural failure in case of turbulence. However, the results also hold for the other states of the wing sections across the wingspan.

B. Comparison Study

A comparison is conducted in this paper to determine the best approach by comparing the reduced model and the true model's behavior of Wing Model 1 and 2 excited by a stochastic Gaussian gust with a frequency of sampling of 100 Hz for 100 seconds. In order to quantify the performance of each approach in the time-domain, the model reduction success is observed from the lowest model realization that can be achieved with a high R^2 value.

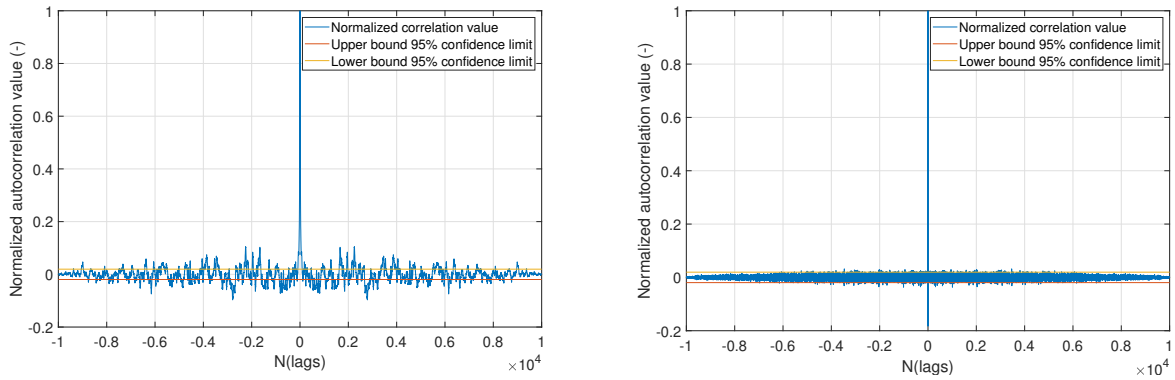

(a) MFLMR balanced truncation without singular perturbation step. **(b) MFLMR balanced truncation with singular perturbation step.**

Figure 9 Normalized error autocorrelation periodogram of reduced model (20 states) against the number of sample lags of Wing Model 1.

1. Model 1

The first results presented are from the Simulation of Model 1, with the perturbation of stochastic Gaussian gust signals. Based on the iteration of balanced truncation realization, it is obtained that the high R-squared (R^2) value of higher than 0.9995 is achieved up to model reduction up to 4 states remaining and higher than 0.995 for the reduced model realization with two states only. Both are achieved in the case of the MFLMR's balanced truncation method with and without singular perturbation step. However, a more stark contrast is observed in terms of normalized error autocorrelation of the simulation. The error ($e(t)$) itself is defined as the difference between the reduced model and true model response at the same timestamp, or

$$e(t) = x_{red} - x_{true} \tag{22}$$

Autocorrelation of the normalized error response can then be calculated across the spectrum. The autocorrelation of normalized error for discrete system is calculated as

$$R_{ee} = \frac{1}{N-1} \sum_{n=0}^{N-1} e(t)e(t-\tau) \tag{23}$$

where τ represents the lag of the sample. The resulting normalized error autocorrelation periodogram can then be used as the validation tool. In order to judge the validity of the reduced model, a certain percentage of the normalized error sample must be within the boundary of confidence interval. In term of statistics, a confidence interval of 95% is commonly used to determine the validity. In such case, the normalized error autocorrelation value is ideally bounded at

$$\alpha_{95} = \frac{1.96}{\sqrt{N}} \tag{24}$$

The sample provided is from the reduced model realization of 20 states can be observed from Figure 9 that both periodograms possess the same characteristics where the maximum is located N=0 where autocorrelation is maximum at 1. The most important discovery on this plot is that the normalized autocorrelation across the periodogram is more degraded or out of the 95% confidence limit when the singular perturbation step is not applied. This is evident by the position of "white noise" error autocorrelation, which goes beyond the confidence interval boundary. On the other hand, the singular perturbation step's implementation shows that the noise across the periodogram is mostly within the confidence interval boundary. Even at the reduced realization of 10 states (Figure 10), the error autocorrelation shows that the band of error is smaller by applying the singular perturbation step. This signifies that the application of singular perturbation with modified limited frequency balanced truncation is statistically more acceptable as the error that arises is within the confidence interval. Similar results are also found up to the reduced model of the 4th-order where the R-squared value is higher than 0.9995.

The rule of the validity is then determined on how many points across the periodogram fall within the confidence interval boundary. In other words, if 95% confidence interval is established, a valid reduced model will have 95%

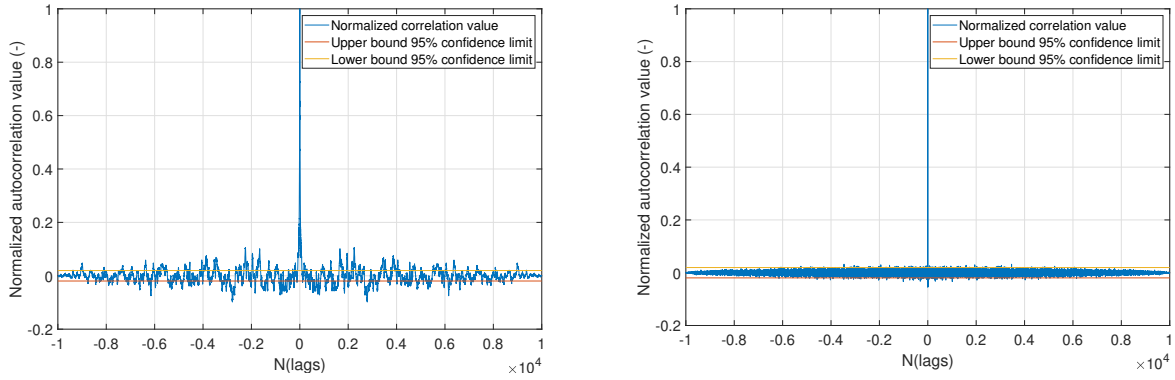

(a) MFLMR balanced truncation without singular perturbation step. **(b) MFLMR balanced truncation with singular perturbation step.**

Figure 10 Normalized error autocorrelation periodogram of reduced model (10 states) against the number of sample lags of Wing Model 1.

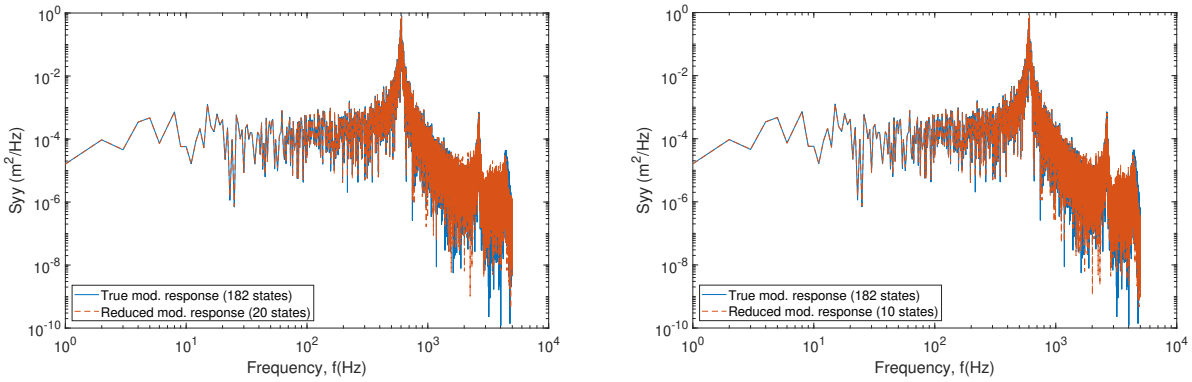

(a) PSD of true model (182 states) and reduced model (20 states). **(b) PSD of true model (182 states) and reduced model (10 states).**

Figure 11 Power Spectral Density comparison between the true model and the reduced models of Wing Model 1.

of periodogram points within the bound established at Equation 24 [46] as this means that the error occurring to the calculation is white noise and therefore the reduced model is the reliable representation of the true model. Given the results of the normalized error autocorrelation periodograms, the data shows that 58.16% and 57.93% of the data is within the confidence interval limit for the reduced model with respectively 20 states and 10 states without singular perturbation step. This signifies that the occurring error between the reduced and the true model is not only white noise. On the other hand, the error autocorrelation for the reduced model with singular perturbation step achieves the score of 98.28% and 98.55% within confidence interval for reduced realization with 20 and 10 states respectively.

The analysis of the error autocorrelation periodogram is further supported by the analysis of power spectral density (PSD) of both the true model of 182 states and the reduced model. Although degradation of PSD quality of reduced model realization of 10 states occurs on higher frequencies, it can be seen in Figure 11 that the results for both reduced model realization of 20 states and ten states have a similar PSD resembling the true response across the frequency spectrum. Again, by comparing the PSD of the reduced model of 10 states with (Figure 11b) or without the singular perturbation model (Figure 12). It can be seen that a slight deviation occurs at a lower frequency. This signifies that the reduced model is not able to capture the modes at that frequency accurately, and the error therefore is not white noise. However, looking at the PSD chart, it can be seen that the reduced model response can follow the trend of the true model albeit not as accurate as the results with the extension of singular perturbation step. This may explain the occurrence of more prominent error autocorrelation when the singular perturbation assumption is not applied despite the success in the time-domain analysis. Here the singular perturbation adjusts the frequency response at the lower frequency. The same results for MFLMR with singular perturbation case can also be observed from the reduced model's PSD of a smaller order, i.e., 5th order and 2nd order as presented in Figure 13. In these cases, both reduced models' PSDs do

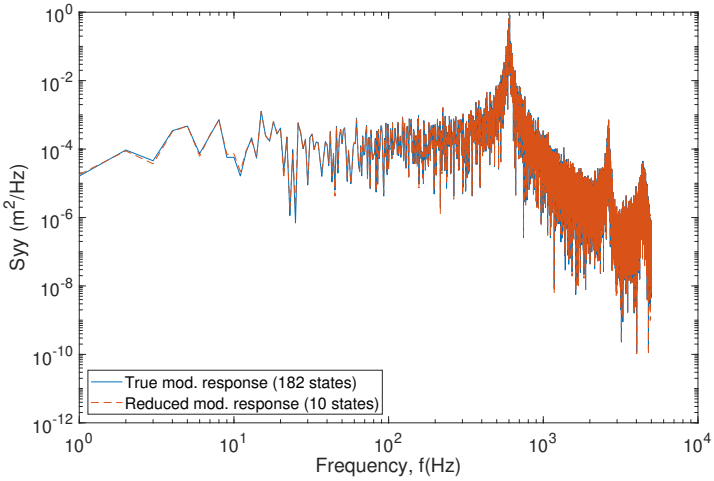

Figure 12 PSD of true model (182 states) and reduced model (10 states) without singular perturbation step at lower frequency.

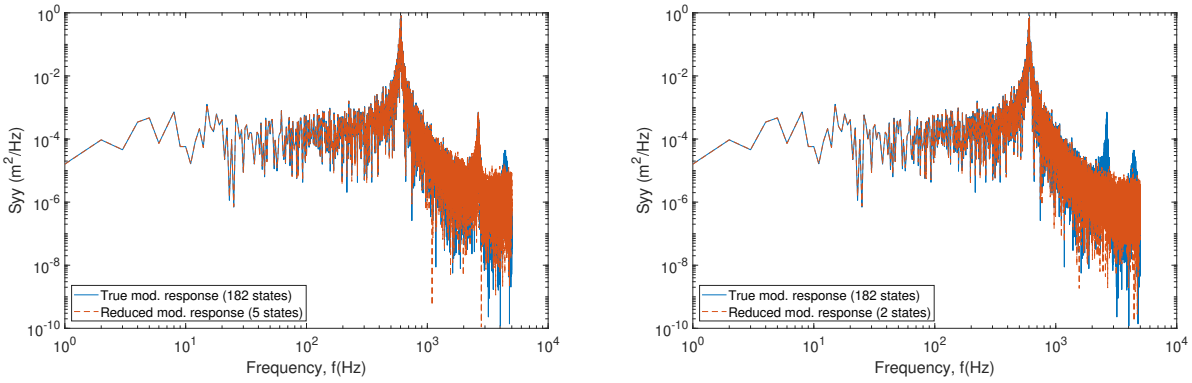

(a) PSD of true model (182 states) and reduced model (5 states). **(b) PSD of true model (182 states) and reduced model (2 states).**

Figure 13 PSD comparison between the true model and the reduced models with very small order of Wing Model 1 with singular perturbation.

not follow the system's frequency response at a very high frequency above 1000 Hz which reflects in the decrease of the R-squared value of the reduced model simulation results. Given the evidence, it can be seen that the singular perturbation step application with the MFLMR method gives better results in both frequency and time domain as it can capture the behavior of the true model at the determined frequency with less error.

2. Model 2

The R-squared and normalized error autocorrelation comparison are presented to the Asjes' damping case for Model 2. Using the same means of measurements and observation for the previous model, few same characteristics can be found. With the singular perturbation step, the resulted state space of MFLMR's balanced truncation can achieve a high R-squared value (between 0.995 and less than 1) up to the realization of 11 states where perfect agreement with the true model is met at the reduced model of the 12th order or higher. More states are required when the singular perturbation step is not used, the perfect R-squared value is attained at the reduced realization of 17 states, but the high R-squared value is attained up to the reduced realization of 10 states. Therefore it can be seen that the results in the time domain analysis are again comparable. Using the normalized error autocorrelation periodogram again, the noise across the periodogram is beyond the confidence interval boundary with the realization using the pure MFLMR's balanced

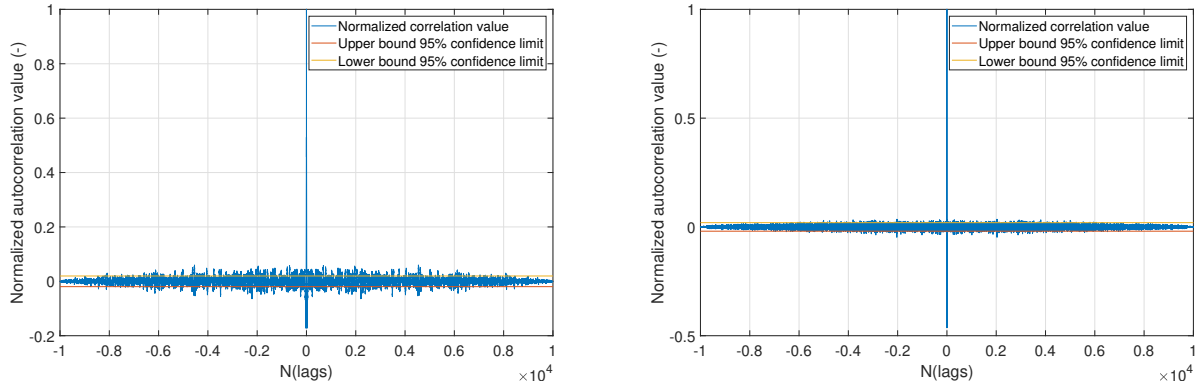

(a) MFLMR balanced truncation without singular perturbation step. **(b) MFLMR balanced truncation with singular perturbation step.**

Figure 14 Normalized error autocorrelation periodogram of reduced model (20 states) against the number of sample lags of Wing Model 2.

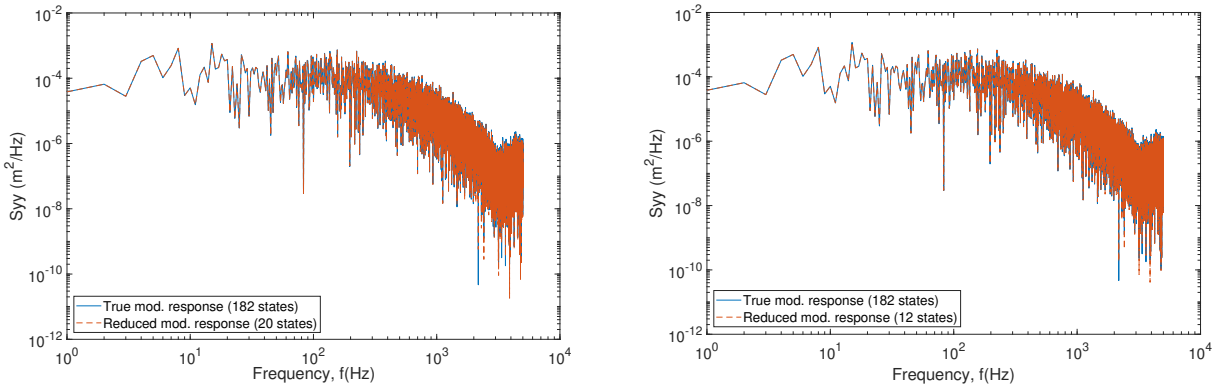

(a) PSD of true model (182 states) and reduced model (20 states). **(b) PSD of true model (182 states) and reduced model (12 states).**

Figure 15 Power Spectral Density comparison between the true model and the reduced models of Wing Model 2.

truncation. This is evident as the error autocorrelation is more pronounced without applying the singular perturbation step, even at the perfect R-squared reduced model, i.e., reduced realization with 20 states remaining in Figure 14, where only 81.5% of the samples of the pure MFLMR are within the 95% confindence interval limit in constrast with 96.86% with the application of singular perturbation step. This signifies that the error occurring from the model reduction without singular perturbation is not white noise, which makes the result not reliable. Again by using PSD analysis, the results show a resemblance between the true and reduced model, e.g., the reduced model realization of 12 and 20 states as in Figure 15. Therefore, it can be supported that implementing the singular perturbation step is beneficial to enhance the quality of model reduction.

Given the comparison study above, it can be inferred that the MFLMR's frequency-limited balanced truncation with singular perturbation step yields the best results at the limited-frequency model reduction case based on the measurement of the normalized error autocorrelation and PSD periodogram in the frequency domain, and the R-squared value of the reduced model in the time domain. However, it is noteworthy that the complexity or the linearity of the model becomes the decisive point for the MFLMR algorithm to reduce the system to the smallest possible order. It can be observed that Model 1 can be reduced to 2 states while Model 2 can only be reduced up to 11 states. From these preliminary analyses, it can be further recommended that the implementation of the proposed model reduction method can be applied to the state and parameter estimation in order to maintain the high sample rate that can be attained by using the controller scheme with visual tracking in order to yield an accurate solution for the aeroelastic wing controller feedback. The reduced model's application in the system identification with high frame rate visual tracking will be reported in the further report.

V. Conclusion

In this paper, a full analysis is conducted to provide a model reduction solution for state and parameter estimation routine as a part of an aeroelastic controller scheme with visual tracking for online structural state control to maintain the wing's integrity fluttering conditions. The proposed model reduction method is called the Modified Frequency-Limited Model Reduction (MFLMR) routine. As the model reduction success depends on the state energy distribution, an additional singular perturbation step can be used to improve the model reduction results at the declared operating frequency band as the operating limit is at lower frequency. A simulation of gust with stochastic Gaussian forces and moments are conducted for two models of the wing. The results reveal that the proposed MFLMR method with singular perturbation step succeeds in obtaining reduced model realization provides more reliable results based on the error autocorrelation compared to the true model in the same realization for Model 1 with the reduced model of MFLMR without the singular perturbation addition. The same results were also obtained for the simulation with Model 2. From the overall results, it can be concluded that the MFLMR can estimate the true displacement of the wing section, and the singular perturbation step allows a more accurate result in the frequency domain. However, it is noteworthy that the complexity or the linearity of the model becomes the decisive point for the MFLMR algorithm to reduce the system to the smallest possible order. From these analyses, it can be further recommended that the implementation of the proposed model reduction method can be applied to the state and parameter estimation in order to maintain the high sample rate that can be attained by using the controller scheme with visual tracking in order to yield an accurate solution for the aeroelastic wing controller feedback.

VI. Acknowledgements

The writers would like to thank the Department of Aerospace Structures and Materials, Delft University of Technology, The Netherlands, that facilitated the paper's working and completion.

References

[1] Patil, M. J. and Hodges, D. H., "Flight Dynamics of Highly Flexible Flying Wings," *Journal of Aircraft, November-December 2006*, Vol. 43, No. 6, 2006, pp. 1790–1799.

[2] John, H., "Critical Review of Methods to Predict the Buffet Capability of Aircraft, AD-A008 593," Tech. rep., Messerschmitt-Boelkow-Blohm G.m.b.H, 1974.

[3] Inman, D. J., *Engineering Vibration*, Prentice-Hall, Inc., 2001.

[4] Burner, A. W. and Tian-shu, L., "Videogrammetric Model Deformation Measurement Technique," *Journal of Aircraft*, Vol. 38, 2001, pp. 745–754.

[5] Corke, P. I., "Visual Control of Robot Manipulators – a Review," *Visual Servoing: Real-Time Control of Robot Manipulators Based on Visual Sensory Feedback*, World Scientific, 1993, pp. 1–31.

[6] Wang, X., "Intelligent multi-camera video surveillance: A review," *Pattern recognition letters*, Vol. 34, No. 1, 2013, pp. 3–19.

[7] Belbachir, A. N., *Smart cameras*, Vol. 2, Springer, 2010.

[8] Mkhoyan, T., de Visser, C. C., and De Breuker, R., "Adaptive Real-Time Clustering Method for Dynamic Visual Tracking of Very Flexible Wings," *AIAA Scitech 2020 Forum*, American Institute of Aeronautics and Astronautics (AIAA), jan 2020, p. 2250.

[9] Mkhoyan, T., de Visser, C. C., and De Breuker, R., "Parallel Real-Time Tracking and 3D Reconstruction with TBB for Intelligent Control and Smart Sensing Framework," *AIAA Scitech 2020 Forum*, American Institute of Aeronautics and Astronautics (AIAA), jan 2020, p. 2252.

[10] Lucas, B. D. and Kanade, T., "An Iterative Image Registration Technique with an Application to Stereo Vision," *International Joint Conference on Artificial Intelligence*, 1981, pp. 674–679.

[11] Shi, J. and Tomasi, C., "Good Features to Track," *IEEE Conference on Computer Vision and Pattern Recognition*, 1994, pp. 593–600.

[12] Dorin Comaniciu, V. R. and Meer, P., "Kernel-Based Object Tracking," *IEEE Transactions on Pattern Analysis and Machine Intelligence*, Vol. 25, No. 5, 2003, pp. 564–577.

[13] Henriques, J. F., Caseiro, R., Martins, P., and Batista, J., "High-Speed Tracking With Kernelized Correlation Filters," *IEEE Transactions On Pattern Analysis and Machine Intelligence*, Vol. 37, No. 3, 2014, pp. 583–596.

[14] Huynh, X.-P., Choi, I.-H., and Kim, Y.-G., "Tracking a Human Fast and Reliably Against Occlusion and Human-crossing," *Image and Video Technology*, Springer, 2015, pp. 461–472.

[15] Funk, N., "A Study of The Kalman Filter Applied to Visual Tracking," *University of Alberta, Project for CMPUT*, Vol. 652, No. 6, 2003.

[16] Cuevas, E., Zaldivar, D., and Rojas, R., "Kalman Filter for Vision Tracking, Technical Report B 05-12," Tech. rep., Freie Universitaet Berlin, Institut fuer Informatik, Berlin, Germany, 2005.

[17] Rodriguez, A., Panza, J., Kumar, B. V., and Mahalanobis, A., "Automatic recognition of multiple targets with varying velocities using quadratic correlation filters and Kalman filters," *IEEE Radar Conference*, 2010, pp. 446–451.

[18] Ghanem, R. and Shinozuka, M., "Structural-System Identification I: Theory," *ASCE Journal of Engineering Mechanics*, Vol. 121, No. 2, 1994, pp. 255–264.

[19] Shinozuka, M. and Ghanem, R., "Structural System Identification II: Experimental Verification," *Journal of Engineering Mechanics*, Vol. 121, No. 2, 1995, pp. 265–273.

[20] Grauer, J. A. and Morelli, E. A., "A New Formulation of the Filter-Error Method for Aerodynamic Parameter Estimation in Turbulence," , pp. 2704.

[21] Mulder, J. A., *Design and Evaluation of Dynamic Flight Test Maneuvers*, Ph.D. thesis, Delft University of Technology, 1986.

[22] Theodorsen, T., "General Theory of Aerodynamic Instability and The Mechanism of Flutter," Tech. rep., National Advisory Committee for Aeronautics, United States of America, 1949.

[23] Verboven, P., B.Cauberghe, Guillaume, P., Vanlanduit, S., and Parloo, E., "Modal Parameter Estimation and Monitoring for Online Flight Flutter Analysis," *Mechanical Systems and Signal Processing 18*, Vol. 18, No. 3, 2004, pp. 587–610.

[24] Timme, S. and Sartor, F., "Passive Control of Transonic Buffet Onset on A Half Wing-Body Configuration," *International Forum on Aeroelasticity and Structural Dynamics*, 2015.

[25] Leishman, J. and Nguyen, K., "State-Space Representation of Unsteady Airfoil Behavior," *American Institute of Aeronautics and Astronautics (AIAA) Journal*, Vol. 28, No. 5, 1990, pp. 836–844.

[26] de Breuker, R., Binder, S., and Wildschek, A., "Combined Active and Passive Loads Alleviation through Aeroelastic Tailoring and Control Surface/Control System Optimization," 2018.

[27] Asjes, D. C., *Nonlinear analysis of a two- and three-degree-of-freedom aeroelastic system with rotational stiffness free-play*, Ph.D. thesis, Iowa State University, 2015.

[28] Gillebaart, E. and De Breuker, R., "Reduced-order modeling of continuous-time state-space unsteady aerodynamics," *53rd AIAA Aerospace Sciences Meeting*, 2015, p. 0260.

[29] Besselink, B., Tabak, U., Lutowska, A., Van de Wouw, N., Nijmeijer, H., Rixen, D. J., Hochstenbach, M., and Schilders, W., "A comparison of model reduction techniques from structural dynamics, numerical mathematics and systems and control," *Journal of Sound and Vibration*, Vol. 332, No. 19, 2013, pp. 4403–4422.

[30] Davison, E., "A method for simplifying linear dynamic systems," *IEEE Transactions on automatic control*, Vol. 11, No. 1, 1966, pp. 93–101.

[31] Hall, K. C., "Eigenanalysis of unsteady flows about airfoils, cascades, and wings," *AIAA journal*, Vol. 32, No. 12, 1994, pp. 2426–2432.

[32] Moore, B., "Principal component analysis in linear systems: Controllability, observability, and model reduction," *IEEE transactions on automatic control*, Vol. 26, No. 1, 1981, pp. 17–32.

[33] Holmes, P., Lumley, J. L., Berkooz, G., and Rowley, C. W., *Turbulence, coherent structures, dynamical systems and symmetry*, Cambridge university press, 2012.

[34] Willcox, K. and Peraire, J., "Balanced model reduction via the proper orthogonal decomposition," *AIAA journal*, Vol. 40, No. 11, 2002, pp. 2323–2330.

[35] Rowley, C. W., "Model reduction for fluids, using balanced proper orthogonal decomposition," *International Journal of Bifurcation and Chaos*, Vol. 15, No. 03, 2005, pp. 997–1013.

[36] Odabasioglu, A., Celik, M., Pileggi, L. T., Pileggi, L. T., and Pileggi, L. T., "PRIMA: Passive reduced-order interconnect macromodeling algorithm," *Proceedings of the 1997 IEEE/ACM international conference on Computer-aided design*, IEEE Computer Society, 1997, pp. 58–65.

[37] Saad, Y., *Iterative methods for sparse linear systems*, Vol. 82, siam, 2003.

[38] Gressick, W., Wen, J. T., and Fish, J., "Order reduction for large-scale finite element models: A systems perspective," *International Journal for Multiscale Computational Engineering*, Vol. 3, No. 3, 2005.

[39] Laub, A., Heath, M., Paige, C., and Ward, R., "Computation of system balancing transformations and other applications of simultaneous diagonalization algorithms," *IEEE Transactions on Automatic Control*, Vol. 32, No. 2, 1987, pp. 115–122.

[40] Enns, D. F., "Model reduction with balanced realizations: An error bound and a frequency weighted generalization," *The 23rd IEEE conference on decision and control*, IEEE, 1984, pp. 127–132.

[41] Gawronski, W. and Juang, J.-N., "Model reduction in limited time and frequency intervals," *International Journal of Systems Science*, Vol. 21, No. 2, 1990, pp. 349–376.

[42] Gugercin, S. and Antoulas, A. C., "A survey of model reduction by balanced truncation and some new results," *International Journal of Control*, Vol. 77, No. 8, 2004, pp. 748–766.

[43] Tol, H., *Finite-dimensional approximation and control of shear flows*, Ph.D. thesis, Delft University of Technology, 2018.

[44] Kokotovic, P. V., O'Malley Jr, R. E., and Sannuti, P., "Singular perturbations and order reduction in control theory—an overview," *Automatica*, Vol. 12, No. 2, 1976, pp. 123–132.

[45] Werter, N. P. M., *Aeroelastic Modelling and Design of Aeroelastically Tailored and Morphing Wings*, Ph.D. thesis, Delft University of Technology, 2017.

[46] Box, G. and Jenkins, G., *Time series analysis: forecasting and control*, Holden-Day series in time series analysis, Holden-Day, 1970.